Energy Storage Materials 44 (2022) 425–432

Contents lists available at ScienceDirect

Energy Storage Materials

journal homepage: www.elsevier.com/locate/ensm

Achieving reversible precipitation-decomposition of reactive Li_2S towards high-areal-capacity lithium-sulfur batteries with a wide-temperature range

Pan Zeng[a], Cheng Yuan[a], Jiao An[b], Xiaofei Yang[c], Chen Cheng[a], Tianran Yan[a], Genlin Liu[a], Ting-Shan Chan[d], Jun Kang[b,*], Liang Zhang[a,*], Xueliang Sun[c,*]

[a] Institute of Functional Nano & Soft Materials (FUNSOM), Jiangsu Key Laboratory for Carbon-Based Functional Materials & Devices, Soochow University, 199 Ren'ai Road, Suzhou 215123, China
[b] Beijing Computational Science Research Center, Beijing 100193, China
[c] Department of Mechanical and Materials Engineering, University of Western Ontario, London, Ontario N6A 5B9, Canada
[d] National Synchrotron Radiation Research Center, Hsinchu 30076, Taiwan

ARTICLE INFO

Keywords:
Lithium-sulfur batteries
Dual-directional catalysis
Polysulfide redox conversion
Reactive Li_2S

ABSTRACT

Facilitating polysulfide conversion by electrocatalysis is a promising strategy to suppress shuttle effect in lithium-sulfur (Li-S) batteries, yet the active sites in electrocatalysts are gradually passivated by continuous formation of Li_2S passivation layer over cycling, making it challenging to achieve steady conversion of sulfur species. Herein, a strategy of reactive Li_2S collaborated with dual-directional Fe_3C electrocatalyst is proposed to achieve fast and continuous conversion of sulfur species for drastically boosting the performance of Li-S batteries. During the reduction process, reactive Li_2S with unique three-dimensional porous structure is precipitated on Fe_3C surface, which not only shortens ion/electron diffusion path but also exposes and retains more active sites in Fe_3C. While for the following oxidation process, Fe_3C also promotes the decomposition of reactive Li_2S to refresh electrocatalyst surface. Therefore, the high catalytic activity of Fe_3C is well retained during the entire electrochemical process, as verified by comprehensive experimental and theoretical calculation results. Eventually, Fe_3C enables stable operation of high-areal-capacity Li-S batteries (> 6.0 mAh cm^{-2}) under a wide-temperature range (-10 to 40 °C). Our strategy of coupling reactive Li_2S with a bidirectional electrocatalyst provides a new avenue for developing high-energy and wide-temperature Li-S batteries.

1. Introduction

Lithium-sulfur (Li-S) batteries are considered as one of the most promising candidates for next-generation energy storage systems, due to their high theoretical specific energy (2600 Wh kg^{-1}) as well as the use of environment-friendly and low-cost sulfur as the cathode material [1–4]. However, the practical application of Li-S batteries is severely inhibited by the inferior capacity and poor cycling stability resulted from the shuttling of polysulfides, as comprehensively reviewed in our previous reports [5,6]. Strategies of physical restriction and chemical entrapping of polysulfides by a variety of porous carbon materials [7–10], non-carbon materials [11,12], and their hybrids [13] have been widely employed to address above issues. Nonetheless, the sluggish redox conversion of dissolved polysulfides still results in their aggregation in the electrolytes, and therefore, the above-mentioned strategies can only afford a limited ability to restrain the shuttling of polysulfides.

Recently, the utilization of electrocatalyst materials, such as metal oxides (Ta_2O_5 [14], $NiMoO_4$ [15]), phosphides ($Ni_2Co_4P_3$ [16], Ni-Fe-P [17]) and sulfides (ZnS-SnS [18], SnS_2 [19]), to accelerate polysulfide redox kinetics has been regarded as an effectively alternative strategy. However, the solution-mediated precipitation chemistry often leads to the uncontrollable and uneven growth of Li_2S evolved from the dissolved polysulfides [20]. Once a thick and dense Li_2S passivation layer is formed on the electrocatalyst surface during the repeated discharging, the active sites will be deactivated and inaccessible for the following reactions of sulfur cathodes (Fig. 1a), leading to the accumulation of inactive sulfur species in each cycle and thus the structure degradation and capacity fading. The situation gets even worse under practical conditions, such as high sulfur loading, low-temperature, and low electrolyte/sulfur (E/S) ratio.

To avoid the deactivation of electrocatalysts by Li_2S passivation layer, one effective approach is to regulate the Li_2S growth by forming three-dimensional (3D) porous Li_2S (reactive Li_2S) [20–23]. However,

* Corresponding authors.
E-mail addresses: jkang@csrc.ac.cn (J. Kang), liangzhang2019@suda.edu.cn (L. Zhang), xsun9@uwo.ca (X. Sun).

https://doi.org/10.1016/j.ensm.2021.10.035
Received 31 August 2021; Received in revised form 17 October 2021; Accepted 27 October 2021
Available online 29 October 2021

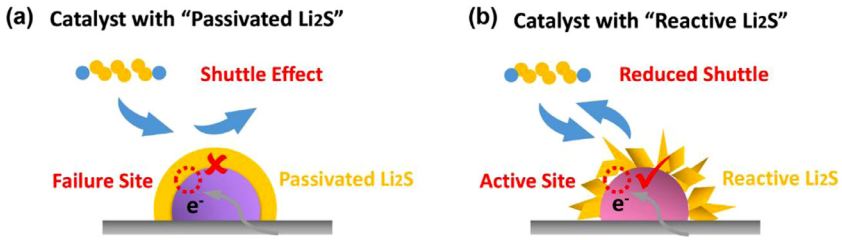

Fig. 1. Schematic illustration of polysulfide conversion on electrocatalyst surface with (a) "passivated Li_2S" and (b) "reactive Li_2S".

the precipitation of reactive Li_2S is mainly implemented by introducing high-donor-number electrolytes [20–23], which results in the poor cycle stability because they have the formidable drawback of extreme reactivity with Li metal anodes. Till now, only few electrocatalysts, e.g., CoS_3 [24], VN [25], Ti_3C_2Tx/polyisoprene [26], and Co phthalocyanine nanorods [27], have been reported with the precipitation of reactive Li_2S. Unfortunately, the utilization of sulfur species and cycle stability of Li-S batteries are still unsatisfactory, owing to the fact that these studies ignore the influence of reactive Li_2S decomposition. If the designed electrocatalyst cannot promote the decomposition of reactive Li_2S, the reactive Li_2S layer will gradually evolve into a dense passivated layer during repeated cycling, owing to the high decomposition barrier of Li_2S. Notably, although dual-directional electrocatalysts such as CoFe [2], TiO_2-Ni_3S_2 heterostructure [3], and $NiMoO_4$ nanosheets [15] have been shown to accelerate the decomposition of Li_2S, the formation of dense and thick Li_2S passivation layer rather than reactive Li_2S is still preferred on these electrocatalyst surfaces. This also leads to the coverage of active sites, reducing the utilization of sulfur species. Therefore, designing an electrocatalyst with enhanced capability of reactive Li_2S precipitation and decomposition, i.e., reactive Li_2S coupled with dual-directional electrocatalyst, is crucial to realize the rapid recycling of polysulfides (Fig. 1b).

Scharifker-Hills model of Li_2S nucleation reveals that fast diffusion of polysulfides and lithium ion (Li^+) afford a spread of polysulfides in 3D space, which is beneficial for Li_2S precipitation with 3D configuration [20,27]. In contrast, a low mobility of polysulfides and Li^+ leads to their localized distribution and the following deposition of Li_2S tends to exhibit a dense and thick manner [28]. Fe_3C has been demonstrated to possess the advantages of low polysulfides and Li^+ diffusion barrier, outstanding conductivity, and superior catalytic activity, along with cost-efficiency and eco-friendly merits [29–31], which is a potential candidate for realizing the facilitated formation and decomposition of reactive Li_2S.

Herein, the precipitation of reactive Li_2S is realized by rational design of Fe_3C@foam carbon/S-carbon fiber cathode (Fe_3C@FC/S-CF), which is remarkably different from the previous reports on the formation of passivated Li_2S layer on Fe_3C surfaces [29–31]. The unique 3D porous structure of Li_2S not only shortens the ion/electron diffusion path, but also guarantees the exposure and retainment of more catalytically active sites of Fe_3C during the electrochemical reaction process. On the other hand, Fe_3C can also serve as a bidirectional electrocatalyst to promote the precipitation and decomposition of Li_2S, which has been largely neglected in previous reports that mainly focus on the monodirectional liquid-solid polysulfide conversion process [25–27]. As a consequence, the high catalytic activity of Fe_3C is well maintained during the entire charge/discharge process, achieving rapid redox conversion of sulfur species, as revealed by comprehensive experimental and theoretical calculation results. Eventually, high-areal-capacity Li-S batteries (> 6.0 mAh cm^{-2}) under a wide-temperature range (-10–40 °C) are achieved via the as-fabricated Fe_3C@FC/S-CF cathode for the first time. Moreover, a high areal capacity of 10 mAh cm^{-2} is retained after 70 cycles under a low E/S ratio of ~8 μL mg^{-1} and high sulfur loading of 16.1 mg cm^{-2} at room temperature. Our work successfully realizes the combination of reactive Li_2S with bidirectional electrocatalyst, which drastically boosts the electrochemical performance of Li-S batteries under practically relevant parameters.

2. Results and discussion

The fabrication process of Fe_3C@FC is illustrated in Fig. 2a. Firstly, urea, glucose, silica sol and iron nitrate nonahydrate were dissolved into distilled water under strong agitation. The obtained mixture solutions were then freeze-dried into a fluffy block. After that, the dry block was calcined at high temperature under inert atmosphere. During the calcination process, the polycondensation of urea generated carbon nitride (C_3N_4) at above 550 °C, acting as the two-dimensional layered template [32]. Simultaneously, the glucose molecules were pyrolyzed into carbon precursor, covering on the surface of two-dimensional C_3N_4 template. As the pyrolysis temperature further increasing, the glucose-derived graphene-like carbon was progressively formed based on the decomposition of layered C_3N_4 [32]. Simultaneously, the dissolution of carbon atoms that permeated into the iron-rich substrate resulted in the formation of Fe_3C nanoparticles at high temperature [29]. Finally, porous Fe_3C@FC composites were fabricated after removing nano-silica. For comparison, pure foam carbon (FC) was also prepared without adding iron nitrate nonahydrate.

Scanning electron microscopy (SEM) image of the as-prepared Fe_3C@FC exhibits a porous foam morphology (Fig. 2b). Transmission electron microscopy (TEM) image further reveals that the Fe_3C@FC microstructure consists of porous wrinkled graphene with embedded Fe_3C nanoparticles (Fig. 2c), and the Fe_3C particles size is mainly distributed in the range of 8–22 nm (Fig. S1). The interplanar spacings measured from high-resolution transmission electron microscopy (HRTEM, Fig. 2d and e) are 0.201 nm, corresponding to the (031) plane of Fe_3C [30]. X-ray diffraction (XRD) peaks shown in Fig. 2f match well with the orthorhombic Fe_3C phase (PDF#77-0255), further indicating the successful preparation of Fe_3C with a high purity. Besides, the high-angle annular dark-field scanning transmission electron microscopy (HAADF-STEM) images and corresponding elemental mappings imply the homogeneous distribution of C and Fe elementals in the Fe_3C nanoparticles (Fig. 2g).

The N_2 adsorption-desorption isotherms of both Fe_3C@FC and FC (Fig. S2a) show the typical type IV curves, confirming their predominantly mesoporous structure. The pore size distributions indicate the relatively concentrated pore size in the range of 2–10 nm (Fig. S2b). Based on the Brunauer-Emmett-Teller (BET) calculations, both Fe_3C@FC and FC exhibit high specific surface areas, which are 622.8 m^2 g^{-1} and 862.9 m^2 g^{-1}, respectively. The relatively low surface area of Fe_3C@FC is attributed to the addition of metal, which increases the density of the composite. The weight percentage of Fe_3C@FC maintains at 11% after 900 °C calcination under air atmosphere (Fig. S3) and the residue after thermogravimetric analysis is Fe_2O_3 [29]. Thus, the weight ratio of Fe_3C in the pristine Fe_3C@FC composite is calculated to be ~8%.

X-ray absorption fine structure (XAFS) was performed to investigate the electronic and local coordination structure of Fe_3C@FC. Fig. 2h shows the Fe K-edge X-ray absorption near-edge structure (XANES) spectra of Fe_3C@FC and Fe foil and Fe_2O_3. The $E_{0.5}$ energy value of Fe_3C@FC lies between that of Fe foil and Fe_2O_3, implying that the valence state of Fe atoms is between Fe^0 and Fe^{3+}. Fe L-edge XANES

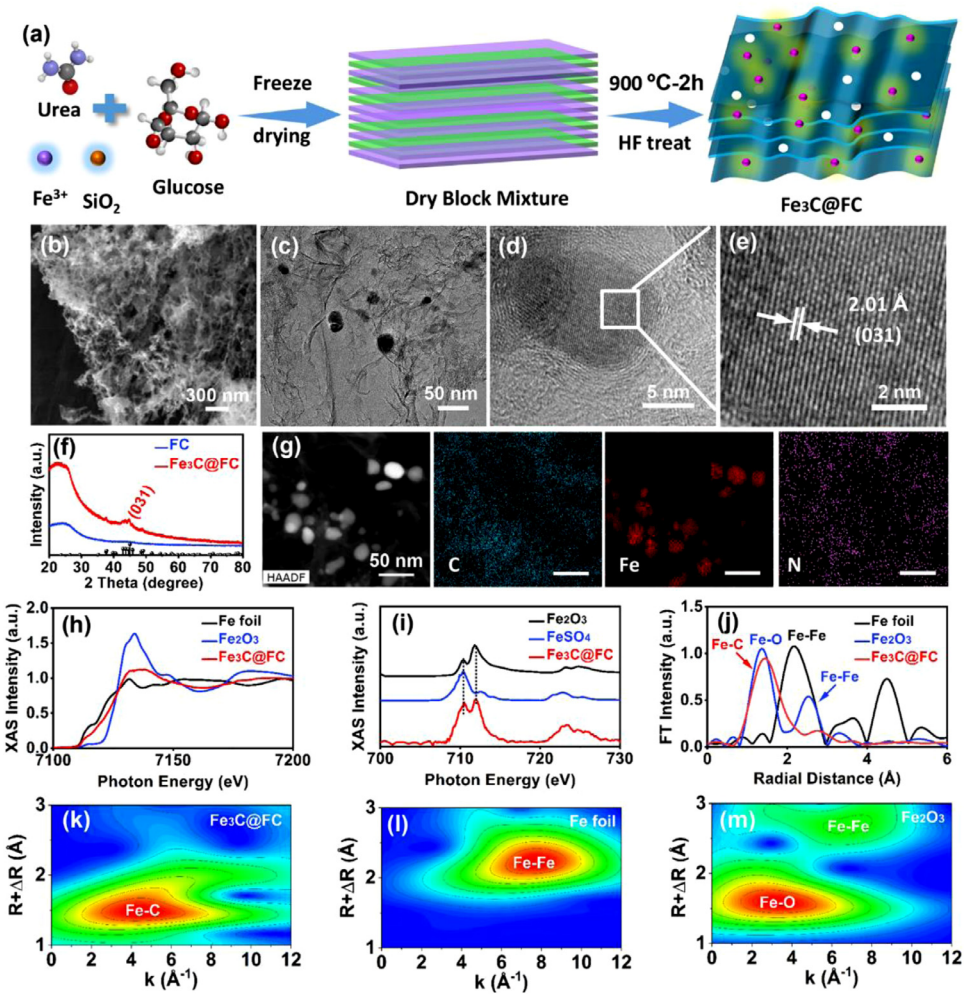

Fig. 2. (a) Schematic illustration of the preparation process of Fe_3C@FC composites. (b) SEM, (c) TEM, (d, e) HRTEM images of Fe_3C@FC composites. (f) XRD patterns of FC and Fe_3C@FC composites. (g) HAADF-STEM and corresponding elemental mapping images of Fe_3C@FC composites. (h) Fe K-edge XANES spectra of Fe_3C@FC, Fe foil, and Fe_2O_3. (i) Fe L-edge XANES spectra of Fe_3C@FC, $FeSO_4$, Fe_2O_3. (j) FT-EXAFS spectra and WT-EXAFS (k-m) of Fe_3C@FC, Fe foil, and Fe_2O_3.

spectra (Fig. 2i) further reveals that the Fe_3C@FC is composed of Fe^{2+} and Fe^{3+} ions, agreeing well with the X-ray photoelectron spectroscopy (XPS) results (Fig. S4) [30]. Moreover, the Fourier-transformed extended X-ray absorption fine structure (FT-EXAFS) profile at Fe K-edge presents only one strong Fe-C peak at ~1.5 Å without the presence of Fe-Fe peak at ~2.1 Å for Fe_3C@FC. The wavelet transform (WT) contour plot further demonstrates the presence of only Fe-C coordination at 4 $Å^{-1}$, in stark contrast to that of Fe foil and Fe_2O_3 (Fig. 2k–m), suggesting the successful preparation of Fe_3C [33,34]. The Fe_3C@FC/S-CF cathode was prepared by titration method (Fig. S5a), with a sulfur content of approximately 89 wt% (Fig. S6). SEM image and energy dispersive spectroscopy (EDS) mappings (Fig. S5b–e) exhibit a uniform sulfur distribution in the as-prepared Fe_3C@FC/S, which ensures the fast reaction of sulfur in the electrochemical reaction process.

To confirm the formation of reactive Li_2S in the actual Li-S battery, the Fe_3C@FC/S-CF cathode after discharging to 1.7 V (Fig. 3a) was characterized by SEM. As shown in Fig. 3b, porous needle-like/sheet-like 3D Li_2S is formed on the surface of Fe_3C@FC/S-CF cathode. In sharp contrast, a dense Li_2S passivation layer is formed on the FC/S-CF surface (Fig. S7a and b). Impressively, after soaking Fe_3C@FC/S-CF and FC/S-CF cathodes (discharging to 1.7 V) into Li_2S_6 solutions for 0.5 h, the color of Li_2S_6 solutions with Fe_3C@FC/S-CF cathode exhibits a lighter pale yellow than that with FC/S-CF cathode (Fig. 3c). These results imply that Fe_3C deposited with reactive Li_2S still preserves and exposes the active site, which is beneficial for the continuous chemisorption and subsequent catalytic conversion of polysulfides. Meanwhile, the unique 3D porous structure of reactive Li_2S also ensures fast Li^+ diffusion. As shown in Figs. 3d, e and S8, the Li^+ diffusion kinetics in different cathodes were explored by cyclic voltammetry (CV) tests at different scan rates (0.05–0.2 mV s^{-1}). For Fe_3C@FC/S-CF cathode, the Li^+ diffusion coefficient (D_{Li}^+) values calculated from Randles-Sevcik equation are higher than that of FC/S-CF cathode, indicating fast Li^+ diffusion on Fe_3C surface (Table S1). Particularly, with a high sulfur loading of 6.9 mg cm^{-2}, the D_{Li}^+ value of cathodic peak at ~2.0 V is close to the reported values with a low sulfur loading [5,7,18], suggesting that the formation of reactive Li_2S indeed ensures an efficient Li^+ diffusion. The improved Li^+ diffusion kinetics mainly derives from two aspects: (i) the Li^+ diffusion barrier is low on Fe_3C surface (0.19 eV), as shown in Fig. 3f and g; (ii) compared with dense Li_2S passivation layer, reactive Li_2S increases the contact area between Li^+ and electrocatalyst, and thus shortens the ion diffusion path. Such fast ion diffusion is in turn beneficial for the precipitation of reactive Li_2S [28]. In addition, the precipitation of reactive Li_2S should be also associated with the open network structure of carbon fibers that provide enough microscopic regions for the nucleation of Li_2S [21,28].

To further validate the role of Fe_3C promoter for Li_2S deposition and growth, potentiostatic discharge experiments were carried out to monitor the Li_2S deposition. As shown in Fig. 3h and i, the nucleation tests show the higher capacity of precipitated Li_2S on Fe_3C@FC–CF (299 mAh g^{-1}) than that on FC–CF (220 mAh g^{-1}), indicating the faster kinetics of Li_2S nucleation and growth for the former. Consistent with above results in Fig. 3b, a dense and thick Li_2S passivation is precipitated on the surface of FC–CF (Fig. 3h), whereas the Li_2S deposited on the Fe_3C@FC–CF surface possesses a loose and flower/needle-like mor-

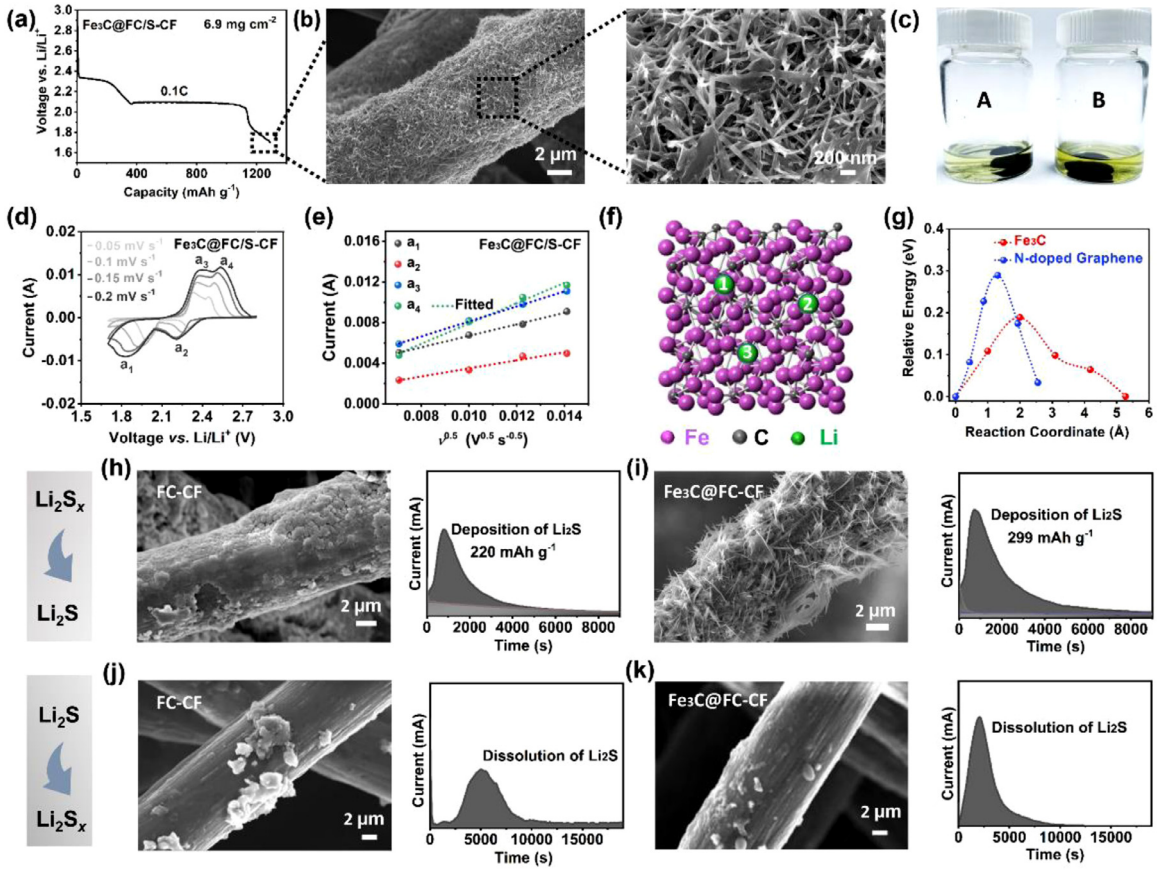

Fig. 3. (a) Discharge curve of Li-S battery using Fe_3C@FC/S-CF cathode with a sulfur loading of 6.9 mg cm^{-2}. (b) SEM images of Fe_3C@FC/S-CF cathode after discharging to 1.7 V. (c) Photograph of Li_2S_6 solutions containing (A) Fe_3C@FC/S-CF and (B) FC/S-CF cathode after discharging to 1.7 V. (d) CV curves at various scan rates with Fe_3C@FC/S-CF cathode and (e) corresponding linear fits of the redox peak currents. (f) Calculated Li-ion diffusion path and (g) diffusion barrier on Fe_3C surface. 1, 2, and 3 represent initial state, transition state, and final state, respectively. Potentiostatic discharge profiles of Li_2S_6 solutions discharged at 2.05 V on (h) FC-–CF and (i) Fe_3C@FC-–CF surfaces. Potentiostatic charge profiles at 2.35 V on (j) FC-–CF and (k) Fe_3C@FC-–CF surfaces. SEM images in Fig. 3h–k show the morphology of Li_2S nucleation and dissolution on FC-–CF and Fe_3C@FC-–CF surfaces.

phology (Fig. 3i). Such a 3D porous structure of reactive Li_2S could not only expose and maintain more active sites of Fe_3C@FC–CF but also shorten the ion/electron diffusion path, which is highly desirable to alleviate cathode passivation toward significantly improved utilization of sulfur species.

The oxidation of Li_2S was also investigated through potentiostatic charging experiments. The decomposition capacity estimated by the quantity of electric charge is much higher for Fe_3C@FC–CF than FC–CF, suggesting the effective oxidation of Li_2S on Fe_3C@FC–CF surface. Meanwhile, SEM images show that the precipitated Li_2S still exists on FC–CF surface after oxide reaction (Fig. 3j), while it almost disappears on Fe_3C@FC–CF surface (Fig. 3k), suggesting the facilitated decomposition of Li_2S on Fe_3C@FC–CF surface during the charging process.

The aforementioned results clearly demonstrate that Fe_3C promotes the precipitation and decomposition of reactive Li_2S, which mainly associate with the liquid-solid and solid-liquid interconversions of polysulfides and Li_2S. Symmetrical cells were assembled by using Fe_3C@FC–CF and FC–CF identical electrodes with Li_2S_6 electrolyte to reveal the liquid-liquid polysulfide redox kinetics. It is apparent that Fe_3C@FC–CF cell displays a higher current density together with a lower charge transfer resistance compared with that of FC–CF cell (Fig. S9), illustrating the faster and more efficient redox conversion between different polysulfides.

The accelerated liquid-liquid, liquid-solid and solid-liquid conversions of polysulfides verify the superior electrocatalytic reactivity of Fe_3C in regulating polysulfide redox kinetics. To better demonstrate the electrocatalytic effect of Fe_3C for actual Li-S batteries, CV measurements of Li-S batteries assembled with Fe_3C@FC/S-CF and FC/S-CF cathodes were performed in the voltage range of 1.7–2.8 V. As shown in Fig. 4a, even under a high sulfur loading of 6.9 mg cm^{-2}, the Li-S batteries still present typical CV profiles with two cathodic peaks (2.2–2.4 V, 1.9–2.1 V) and two anodic peaks (2.2–2.5 V), corresponding to the two-step reduction of sulfur to Li_2S and the reversible oxidation of Li_2S to sulfur [1–3]. Particularly, a much higher current density and positive shift of cathodic peak at about 2.0 V is detected for the Fe_3C@FC/S-CF cathode, demonstrating the enhanced liquid-solid transformation kinetics [18]. Besides, the improved Li_2S decomposition is also confirmed by the negative shift of the anodic peak and enhanced peak current value.

This scenario is further supported by the Tafel plot, which shows a much smaller Tafel slope for the reduction (Fig. 4b, from Li_2S_x to Li_2S) and oxidation (Fig. 4c, from Li_2S to Li_2S_x) processes. These results clear imply that the bidirectional catalytic activity of Fe_3C@FC toward the rapid redox interconversion between polysulfides and Li_2S. EIS spectra also demonstrates the enhanced reaction kinetics of the Fe_3C@FC/S-CF cathode (Figure S10). To further verify the enhanced oxidation kinetics with Fe_3C@FC/S-CF cathode, Li_2S decomposition barrier was calculated using the climbing image-nudged elastic band method. The energy needed for Li_2S decomposition on Fe_3C surface is only 0.31 eV (Fig. 4d), which is much lower than that on nitrogen doped graphene (N-doped graphene) reported in literature (~2.1 eV) [35]. Therefore, as shown in Fig. 4a, the cathode with Fe_3C shows obvious redox peak shift with

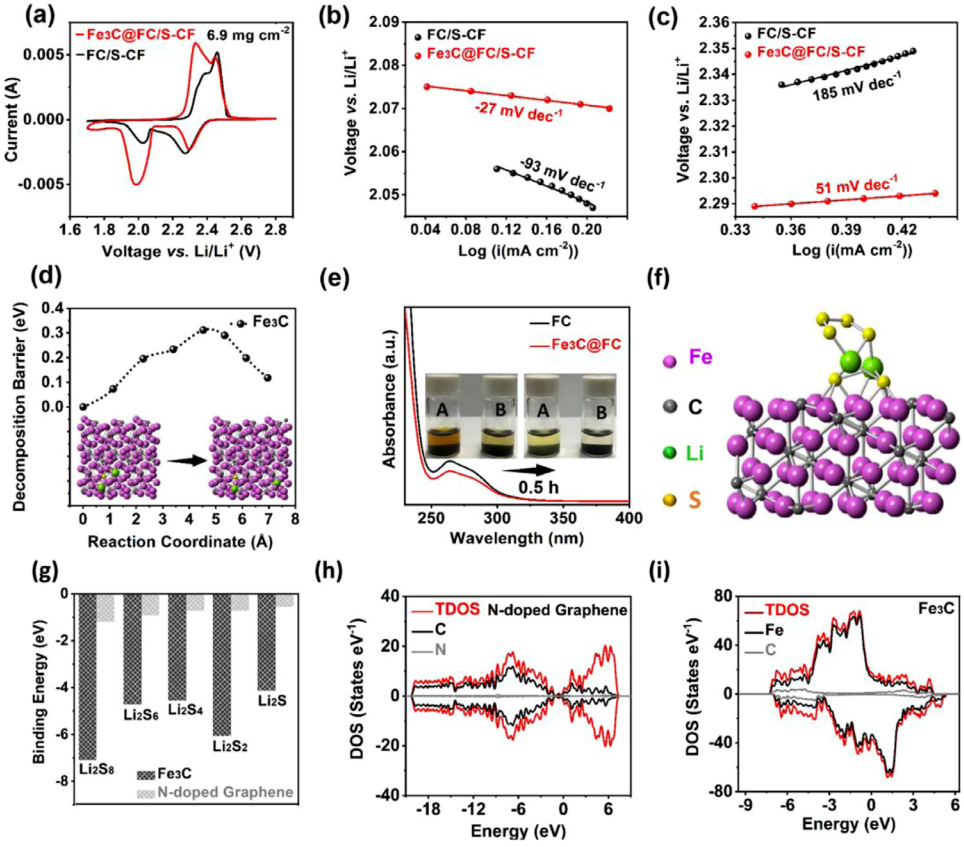

Fig. 4. (a) CV curves of Li-S batteries using different cathodes with a high sulfur loading of 6.9 mg cm^{-2} at a scan rate of 0.05 mV s^{-1}. Tafel plots calculated from (b) the reduction peak at 2.05 V and (c) the oxidation peak at 2.35 V. (d) Li_2S decomposition barriers on Fe_3C surface. (e) UV–vis spectra of Li_2S_6 solutions mixing with Fe_3C@FC and FC powders after 0.5 h. Inset is the photographs of Li_2S_6 solutions containing (A) FC and (B) Fe_3C@FC powders. (f) Geometrically stable configuration of Li_2S_6 adsorbed on Fe_3C surface. (g) Binding energies of Li_2S_x (x = 1, 2, 4, 6 or 8) adsorbed on N-doped graphene and Fe_3C surfaces. DOS patterns of (h) N-doped graphene and (i) Fe_3C, respectively. The Fermi level is set to zero.

much larger current density, suggesting the enhanced precipitation and decomposition of solid Li_2S.

The chemisorption capacity of Fe_3C toward polysulfides is the precondition for realizing their rapid redox conversion. To characterize the chemical interactions between Fe_3C and polysulfides, the visual adsorption experiments were performed in Fig. 4e. The color of Li_2S_6 solutions containing Fe_3C@FC becomes almost transparent, while the color of the solution with FC remains pale yellow after 0.5 h standing. The ultraviolet-visible (UV–vis) spectroscopy of Fe_3C@FC also exhibits a weaker Li_2S_6 absorption peak (250~300 nm) than that of FC, indicating the strong adsorption affinity of Fe_3C@FC toward polysulfides. This phenomenon agrees well with the density functional theory (DFT) calculation results (Fig. 4g), which show a stronger polysulfide adsorption energy for Fe_3C than N-doped graphene because of the formation of Fe-S bonds (Fig. 4f). Moreover, compared to N-doped graphene, the increased density of states (DOS) near the Fermi level of Fe_3C suggests the improved electronic conductivity and reduced activation barrier for electron donation to surface adsorbates (Fig. 4h and i), which should be beneficial for promoting the electrocatalytic activity.

XPS and XAFS characterizations were then performed to explore the valence and chemical environment variation of Fe_3C@FC during the redox reaction process. For the Fe $2p_{3/2}$ XPS spectrum of pristine Fe_3C@FC (Fig. 5a), two characteristic peaks located at 709.7 and 716.9 eV are attributed to Fe^{2+} and Fe^{3+}, respectively [30]. With the increase of the discharge depth, the binding energies of Fe^{2+} and Fe^{3+} downshifts. This is due to the fact that electrons autonomously transfer from polysulfides to the unfilled d orbitals of Fe sites from Fe_3C@FC, resulting in the formation of Fe-S bonding [24]. The related XPS features upshift in the subsequent charge process, indicative of the reversible Fe valence state change. The Fe L-edge XANES spectra (Fig. 5b) consists of two regions, namely L_3 around 709 eV and L_2 around 722 eV, resulting from the core-hole spin-orbital splitting effect. In the following discussion, we will mainly focus on the lineshape evolution of the L_3 edge, which is mainly composed of the t_{2g} state at 710.5 (A_2) and e_g state at 712.1 eV (B_2) [36,37]. The intensity ratio of these multiplet structures is a fingerprint of different oxidation state of Fe (A_2/B_2), which gradually decreases/increases during discharge/charge process, also demonstrating the reversible reduction/oxidation of Fe in Fe_3C. Meanwhile, the Fe K-edge XANES spectra (Fig. 5c) show that the absorption edge energy gradually shifts to lower/higher position during discharge/charge process, further suggesting the reversible Fe valence state variation. Consistent with XPS results, these reversible valence state variation implies Fe_3C can anchor sulfur species and enable the reversible conversion between polysulfides and Li_2S [24]. Besides, the reversible valence change also indicates the chemical and structure stability of Fe_3C, which is of great significance for the continuously catalytic conversion of polysulfides. The corresponding FT-EXAFS spectra (Fig. 5d) reveals the enlargement and shrinkage of Fe-C distance of Fe_3C from 1.5 Å to 1.7 Å and back during the cycling process, as a consequence of the breathing behavior of Fe valence change [36,37]. Importantly, even after 50 cycles (Fig. 5e and f), the reversible behavior is still observed, clearly indicating the well maintenance of the high catalytic activity of Fe_3C over extended cycling with a robust structural stability (Fig. 5g).

Based on the high catalytic activity of Fe_3C with the formation of reactive Li_2S, the potential application of Fe_3C@FC/S-CF in Li-S batteries under practical conditions (i.e., high sulfur loading, low-temperature, and lean E/S ratio) was systematically investigated. We first compare the rate performance of Fe_3C@FC/S-CF and FC/S-CF cathodes with a high sulfur loading of 6.9 mg cm^{-2} and a E/S ratio of ~20 μL mg^{-1} (Fig. 6a). High areal capacities of 7.3, 6.8 and 5.5 mAh cm^{-2} are achieved for Fe_3C@FC/S-CF at 0.1, 0.2 and 0.5 C, respectively, whereas the capacity values are merely 3.2, 3.1 and 2.3 mAh cm^{-2} for FC/S-CF. More particularly, a high areal capacity of 3.5 mAh cm^{-2} is still preserved at a high rate of 1 C for Fe_3C@FC/S-CF. The corresponding charge/discharge voltage profiles of Fe_3C@FC/S-CF exhibit the well-defined voltage plateaus with small polarization potentials (Fig. 6b),

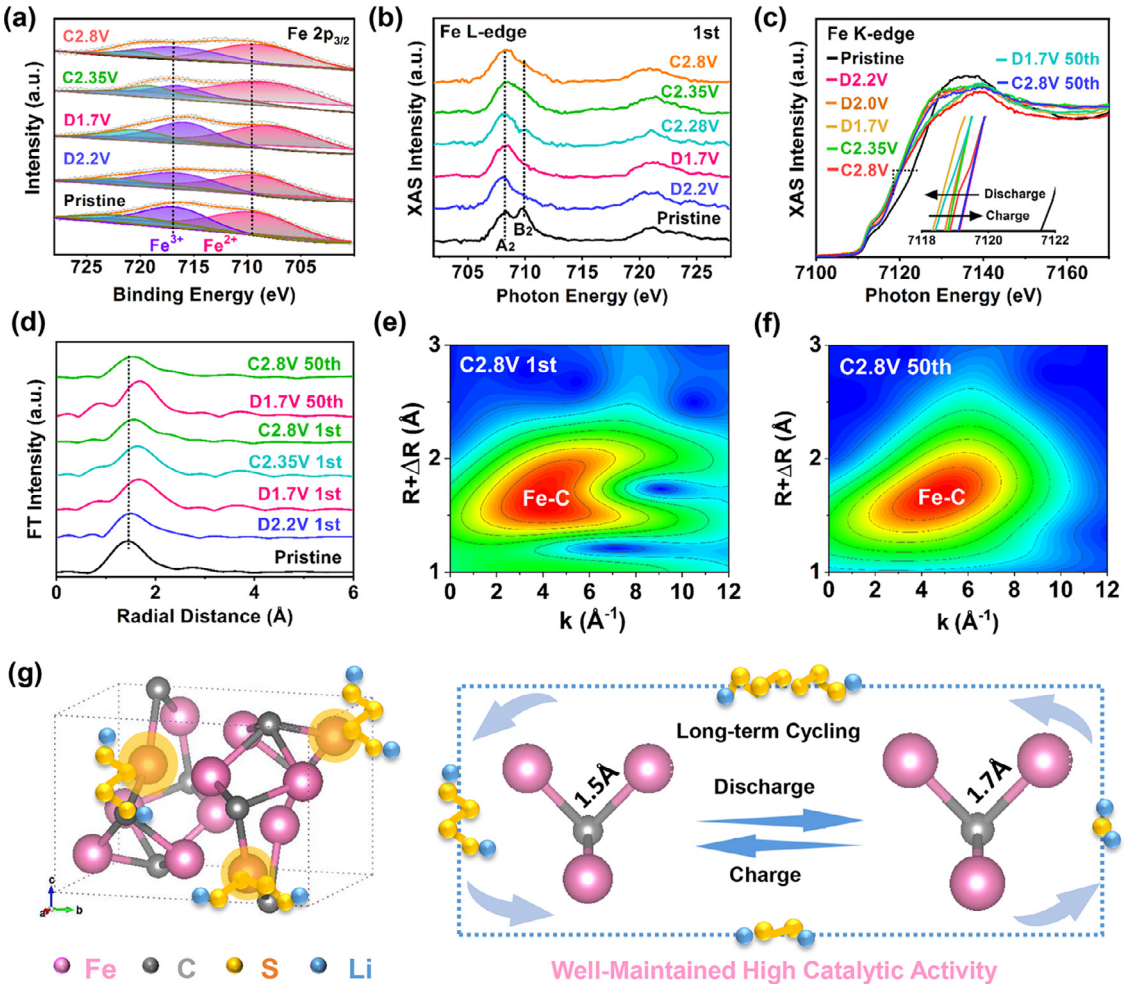

Fig. 5. (a) Fe $2p_{3/2}$ XPS spectra, (b) Fe L-edge XANES spectra, (c) Fe K-edge XANES spectra and (d) corresponding FT-EXAFS spectra of Fe_3C@FC/S-CF at different states of charge. WT transform contour plots of Fe K-edge after (e) 1 and (f) 50 cycles. (g) Variation of Fe_3C structure during the electrochemical reaction process. The reversible change of Fe-C bond length indicates the well-maintained high catalytic activity of Fe_3C.

also demonstrating the enhanced redox kinetics with the addition of Fe_3C. The excellent rate performance with a high sulfur loading should be ascribed to the high catalyst activity of Fe_3C precipitated with reactive Li_2S, which ensures the fast electron/ion diffusion as well as facilitated polysulfide conversion at Fe_3C/electrolyte interface.

The cycling stability of Fe_3C@FC/S-CF and FC/S-CF cathodes with a sulfur loading of 6.9 mg cm^{-2} is compared in Fig. 6c. The initial areal capacity of Fe_3C@FC/S-CF cathode can reach up to 10.3 mAh cm^{-2} (1490 mAh g^{-1}), and then declines slowly to 5.8 mAh cm^{-2} (845 mAh g^{-1}) after 100 cycles with a satisfactory Coulombic efficiency of ~100%. In sharp contrast, the FC/S-CF cathode presents a low areal capacity that is only 3.5 mAh cm^{-2} (510 mAh g^{-1}) after 100 cycles with a low Coulombic efficiency of ~97%. To evaluate the contribution of Fe_3C@FC/S-CF to the observed capacity, cells with lithium anode and pure Fe_3C@FC–CF cathode were assembled and tested under same conditions. As shown in Fig. S11, the capacity of pure Fe_3C@FC–CF without sulfur is only 24 mAh g^{-1}, which can be neglected compared to the high specific capacity of sulfur (1675 mAh g^{-1}). These results indicate that the significant improved capacity of Fe_3C@FC/S-CF originates from the high catalytic active of the Fe_3C accompanied with the reversible precipitation-decomposition of reactive Li_2S, as verified above, establishing a powerful avenue to improve the utilization of sulfur species and thereby effectively suppress the shuttle effect. The effective inhibition of shuttle effect is corroborated by SEM and element analysis of Fe_3C@FC/S-CF cathode and Li anode after 100 cycles (Figs. S12 and S13). Strong sulfur signal is observed from the surface and cross section of Fe_3C@FC/S-CF cathode, implying that polysulfides are effectively entrapped into the Fe_3C@FC/S-CF cathode. Meanwhile, the Li anode with Fe_3C@FC/S-CF cathode exhibits smooth and dense surface (Fig. S13) because of the suppressed shuttle effect, in contrast to that of FC/S-CF cathode.

In addition to high sulfur loading, low-temperature electrochemical performance is also indispensable for the practical Li-S batteries. However, owing to the reduced ion diffusion rate and reaction kinetics at low temperature, the Li-S batteries generally suffer from inferior electrochemical performance even under a low sulfur loading. So far, the research on Li-S batteries with high sulfur loading is mainly focused on room-temperature behavior (~25 °C) and the reported low-temperature Li-S batteries sacrificed the sulfur loading of cathode (only 1~2 mg cm^{-2}) with the achieved areal capacity (0.2~3 mAh cm^{-2}) lower than that of commercial Li-ion batteries (4 mAh cm^{-2}) [38–40]. It is therefore significant to develop Li-S batteries for potential breakthrough at low-temperature performance, particularly under high sulfur loading condition. Herein, taking advantaging of the structural and catalytic properties of Fe_3C, even further increase sulfur loading up to7.8 mg cm^{-2} (Fig. 6d), the Fe_3C@FC/S-CF cathode delivers a high initial areal capacity of up to 7.9 mAh cm^{-2} with a current density of 0.1 C at −10 °C. After 100 cycles, the areal capacity still retains at 5.0 mAh cm^{-2} with a high Coulombic efficiency of ~99%, accompanied with small polariza-

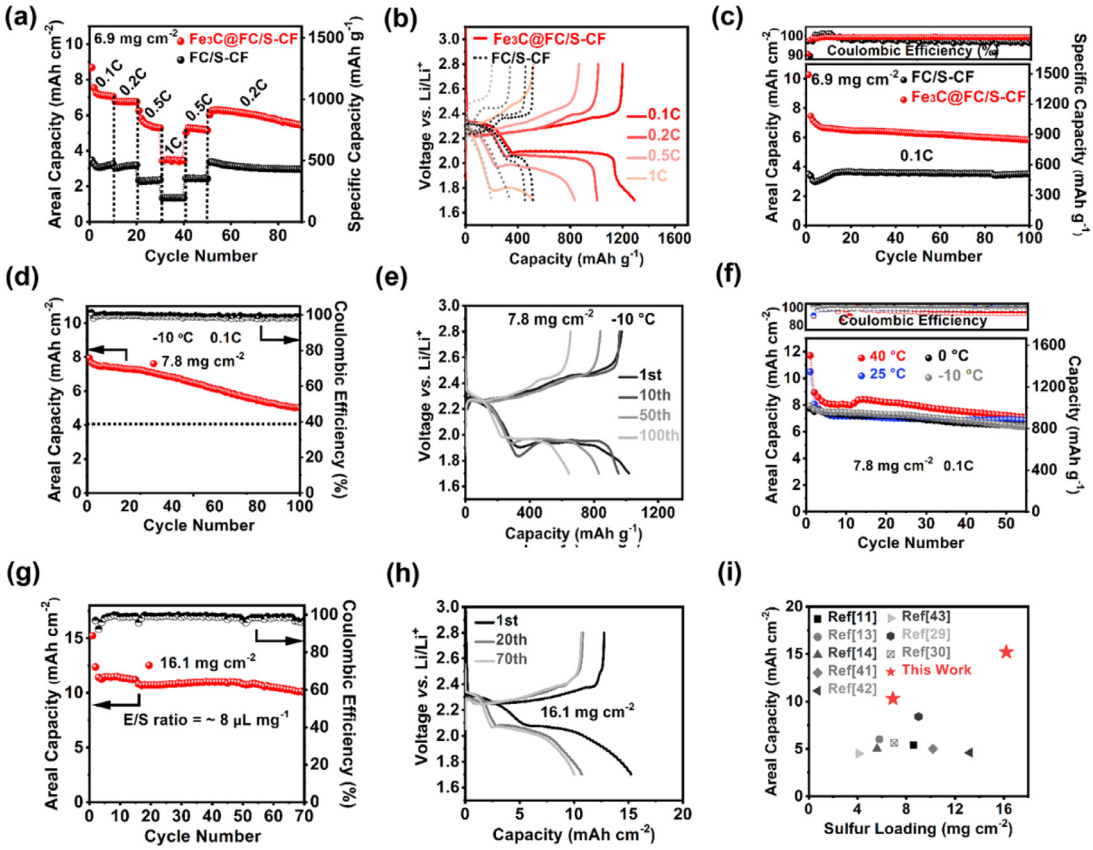

Fig. 6. Electrochemical characterizations of Fe_3C@FC/S-CF and FC/S-CF cathodes. (a) Rate performance, (b) charge/discharge curve and (c) cycle performance of different cathodes with a high sulfur loading of 6.9 mg cm^{-2}. (d) Cycle performance and (e) charge/discharge voltage profiles of Fe_3C@FC/S-CF cathode at −10 °C. (f) Cycle performance of Fe_3C@FC/S-CF cathode with a wide-temperature range. (g) Cycle performance and (h) charge/discharge voltage profiles of Fe_3C@FC/S-CF cathode with a low E/S ratio of ~8 μL mg^{-1} and high sulfur loading of 16.1 mg cm^{-2}. (i) Comparison of areal capacities of high loading cathodes among this work and other literatures.

tion potentials because of the favorable redox kinetics at low temperature (Fig. 6e).

Considering the real application of Li-S batteries in different environments, we have also investigated the cycle performance of Fe_3C@FC/S-CF cathode under a wide-temperature range. As shown in Fig. 6f, stable and high areal capacities of higher than 6 mAh cm^{-2} are obtained in the range of −10 to 40 °C. It is worth mentioning that the dissolution of polysulfides into electrolyte will be accelerated to dissolve into the electrolyte at high temperature, which can exacerbate the shuttle effect and lead to poor cycle stability. Impressively, the areal capacity of up to 7.1 mAh cm^{-2} after 55 cycles is retained for the Fe_3C@FC/S-CF cathode even at a high temperature of 40 °C. Therefore, the improved wide-temperature electrochemical performance enabled by Fe_3C@FC, especially at low-temperature condition, expand the application range of Li-S batteries.

Li-S batteries with both low E/S ratio and high sulfur loading are also highly desired on the way to their commercialization. Here, to make the assembled battery closer to the practical requirements, we further increase the sulfur loading to 16.1 mg cm^{-2} (sulfur content is ~60 wt% in Fe_3C@FC/S-CF, Fig. S14) and reduce the E/S ratio to ~8 μL mg^{-1}, and explore the cycling performance of Fe_3C@FC/S-CF cathode. As shown in Fig. 6g, although increasing sulfur loading to 16.1 mg cm^{-2} under lean electrolyte (~8 μL mg^{-1}), the initial capacity of Fe_3C@FC/S-CF cathode can reach up to 15.2 mAh cm^{-2} at 0.05 C, which preserves at 10 mAh cm^{-2} after 70 cycles. Meanwhile, the batteries still maintain an obvious two-plateau voltage profile after 70 cycles (Fig. 6h), demonstrating the excellent electrochemical reaction kinetics. The high areal capacity of Fe_3C@FC/S-CF cathode outperforms most reported Li-S batteries (Fig. 6i and Table S2), implying its great potential toward Li-S battery practicalization [11,13,14,29,30,41–43]. In addition, we also obtained the high-areal-capacity Li-S batteries with a long cycling stability under low E/S ratio condition (8 μL mg^{-1}). As shown in Fig. S15, the initial capacity of Fe_3C@FC/S-CF cathode can reach up to 9 mAh cm^{-2} at 0.1 C, which is preserved at 4.8 mAh cm^{-2} after 190 cycles. The excellent cycling stability and high areal capacity are ascribed to the high catalytic activity of Fe_3C precipitated with reactive Li_2S, which significantly improves polysulfide conversion kinetics even under high sulfur loading, low temperature and lean E/S ratio conditions.

3. Conclusions

In summary, the reactive Li_2S collaborated with bidirectional Fe_3C electrocatalyst has been proved to be an effective strategy to suppress shuttle effect even under high sulfur loading, low-temperature and lean electrolyte conditions. For the reduction process, reactive Li_2S is precipitated on Fe_3C surface, which exposes and retains more active sites of Fe_3C electrocatalyst as well as ensures fast electron/ion diffusion rate. For the following oxidation process, the decomposition of reactive Li_2S is facilitated by Fe_3C, guaranteeing the refreshment of electrocatalyst surface. Thus, the high electrocatalytic activity of Fe_3C is well retained during the whole charge/discharge process, which leads to the fast and continuous conversion of sulfur species. Therefore, high areal capacity Li-S batteries (> 6 mAh cm^{-2}) under a wide-temperature range (−10–40 °C) are obtained via the as-fabricated Fe_3C@FC/S-CF cathode. In addition, under a low E/S ratio of 8 μL mg^{-1} and high sulfur loading of 16.1 mg cm^{-2}, the initial areal capacity reaches up to 15.2 mAh cm^{-2}

and maintains at 10 mAh cm^{-2} after 70 cycles. The strategy of reactive Li_2S coupled with a bidirectional catalyst provides new perspectives for the development of high-energy and wide-temperature Li-S batteries.

Supporting information

Supporting Information is available from the Online Library or from the author.

Declaration of Competing Interest

The authors declare that they have no competing interests.

CRediT authorship contribution statement

Pan Zeng: Conceptualization, Investigation, Methodology, Data curation, Writing – original draft. **Cheng Yuan:** Conceptualization, Formal analysis. **Jiao An:** Data curation, Methodology, Writing – review & editing. **Xiaofei Yang:** Conceptualization, Writing – review & editing, Validation. **Chen Cheng:** Formal analysis, Data curation. **Tianran Yan:** Formal analysis, Data curation. **Genlin Liu:** Formal analysis, Data curation. **Ting-Shan Chan:** Formal analysis, Data curation. **Jun Kang:** Data curation, Methodology, Investigation. **Liang Zhang:** Conceptualization, Formal analysis, Funding acquisition, Data curation, Investigation, Methodology, Project administration, Resources, Supervision, Validation. **Xueliang Sun:** Conceptualization, Formal analysis, Validation, Supervision, Writing – review & editing.

Acknowledgement

This work is supported by Natural Sciences and Engineering Research Council of Canada (NSERC), Canada Research Chair Program (CRC), and the University of Western Ontario, Collaborative Innovation Center of Suzhou Nano Science & Technology, the 111 project, Joint International Research Laboratory of Carbon-Based Functional Materials and Devices, the National Natural Science Foundation of China (11905154), the Natural Science Foundation of the Jiangsu Higher Education Institutions of China (19KJA550004), the Natural Science Foundation of Jiangsu Province (BK20190814). The authors thank TLS (beamline 01C), NSRL (beamline 11U), SSRF (beamline 02B02 and 11B), and BSRF (beamline 1W1B) for the allocation of synchrotron beamtime.

Supplementary materials

Supplementary material associated with this article can be found, in the online version, at doi:10.1016/j.ensm.2021.10.035.

References

[1] X. Li, M. Banis, A. Lushington, X.F. Yang, Q. Sun, Y. Zhao, C.Q. Liu, Q.Z. Li, B.Q. Wang, W. Xiao, C.H. Wang, M. Li, J.W. Liang, R.Y. Li, Y.F. Hu, L. Goncharova, H. Zhang, T.K. Sham, X.L. Sun, Nat. Commun. 9 (2018) 4509.
[2] Z. Shi, Z. Sun, J. Cai, Z. Fan, J. Jin, M. Wang, J. Sun, Adv. Funct. Mater. 31 (2021) 2006798.
[3] R. Wang, C. Luo, T. Wang, G. Zhou, Y. Deng, Y. He, Q. Zhang, F. Kang, W. Lv, Q.H. Yang, Adv. Mater. 32 (2020) e2000315.
[4] P. Zeng, C. Liu, X. Zhao, C. Yuan, Y. Chen, H. Lin, L. Zhang, ACS Nano 14 (2020) 11558.
[5] X.F. Yang, J. Luo, X.L. Sun, Chem. Soc. Rev. 49 (2020) 2140.
[6] X.F. Yang, X. Li, K. Adair, H. Zhang, X.L. Sun, Electrochem. Energy Rev. 1 (2018) 239.
[7] P. Zeng, L. Huang, X. Zhang, R. Zhang, L. Wu, Y. Chen, Chem. Eng. J. 349 (2018) 327.
[8] Y.Y. Yen, S.H. Chung, Chem. Commun. 57 (2021) 2009.
[9] Y.C. Ho, S.H. Chung, Chem. Eng. J. 422 (2021) 130363.
[10] J.L. Guo, H. Pei, Y. Dou, S.Y. Zhao, G.S. Shao, J.P. Liu, Adv. Funct. Mater. 31 (2021) 2010499.
[11] Y. Wang, R. Zhang, J. Chen, H. Wu, S. Lu, K. Wang, H. Li, C.J. Harris, K. Xi, R.V. Kumar, S. Ding, Adv. Energy Mater. 9 (2019) 1900953.
[12] Z. Shen, Z. Zhang, M. Li, Y. Yuan, Y. Zhao, S. Zhang, C. Zhong, J. Zhu, J. Lu, H. Zhang, ACS Nano 14 (2020) 6637.
[13] Y. Tian, G. Li, Y. Zhang, D. Luo, X. Wang, Y. Zhao, H. Liu, P. Ji, X. Du, J. Li, Z. Chen, Adv. Mater. 32 (2020) e1904876.
[14] Z. Zhang, D. Luo, G. Li, R. Gao, M. Li, S. Li, L. Zhao, H. Dou, G. Wen, S. Sy, Y. Hu, J. Li, A. Yu, Z. Chen, Matter 3 (2020) 1.
[15] T. Sun, X. Zhao, B. Li, H. Shu, L. Luo, W. Xia, M. Chen, P. Zeng, X. Yang, P. Gao, Y. Pei, X. Wang, Adv. Funct. Mater. (2021), doi:10.1002/adfm.202101285.
[16] Z. Shen, M. Cao, Z. Zhang, J. Pu, C. Zhong, J. Li, H. Ma, F. Li, J. Zhu, F. Pan, H. Zhang, Adv. Funct. Mater. 30 (2019) 1906661.
[17] X. Chen, S. Zeng, H. Muheiyati, Y. Zhai, C. Li, X. Ding, L. Wang, D. Wang, L. Xu, Y. He, Y. Qian, ACS Energy Lett. 4 (2019) 1496.
[18] W. Yao, W. Zheng, J. Xu, C. Tian, K. Han, W. Sun, S. Xiao, ACS Nano (2021), doi:10.1021/acsnano.1c00270.
[19] X. Gao, X. Yang, M. Li, Q. Sun, J. Liang, J. Luo, J. Wang, W. Li, J. Liang, Y. Liu, S. Wang, Y. Hu, Q. Xiao, R. Li, T.-K. Sham, X. Sun, Adv. Funct. Mater. 29 (2019) 1806724.
[20] Z. Li, Y. Zhou, Y. Wang, Y.-C. Lu, Adv. Energy Mater. 9 (2019) 1802207.
[21] H. Chu, H. Noh, Y.J. Kim, S. Yuk, J.H. Lee, J. Lee, H. Kwack, Y. Kim, D.K. Yang, H.T. Kim, Nat. Commun. 10 (2019) 188.
[22] M. Baek, H. Shin, K. Char, J.W. Choi, Adv. Mater. 32 (2020) e2005022.
[23] M. Zhao, B.-Q. Li, X. Chen, J. Xie, H. Yuan, J.-Q. Huang, Chem 6 (2020) 3297.
[24] X. Yang, X. Gao, Q. Sun, S.P. Jand, Y. Yu, Y. Zhao, X. Li, K. Adair, L.Y. Kuo, J. Rohrer, J. Liang, X. Lin, M.N. Banis, Y. Hu, H. Zhang, X. Li, R. Li, H. Zhang, P. Kaghazchi, T.K. Sham, X. Sun, Adv. Mater. 31 (2019) e1901220.
[25] S. Tan, Y. Dai, Y. Jiang, Q. Wei, G. Zhang, F. Xiong, X. Zhu, Z.Y. Hu, L. Zhou, Y. Jin, K. Kanamura, Q. An, L. Mai, Adv. Funct. Mater. 31 (2020) 2008034.
[26] T. Lei, Y. Hu, W. Chen, W. Lv, Y. Jiao, X. Wang, X. Lv, Y. Yan, J. Huang, J. Chu, C. Yan, C. Wu, X. Wang, W. He, J. Xiong, Energy Storage Mater. 26 (2020) 65.
[27] X.X. Yang, X.T. Li, C.F. Zhao, Z.H. Fu, Q.S. Zhang, C. Hu, ACS Appl. Mater. Interfaces 12 (2020) 32752.
[28] H. Pan, J. Chen, R. Cao, V. Murugesan, N.N. Rajput, K.S. Han, K. Persson, L. Estevez, M.H. Engelhard, J.-G. Zhang, K.T. Mueller, Y. Cui, Y. Shao, J. Liu, Nat. Energy 2 (2017) 813.
[29] H. Li, S. Ma, H. Cai, H. Zhou, Z. Huang, Z. Hou, J. Wu, W. Yang, H. Yi, C. Fu, Y. Kuang, Energy Storage Mater. 18 (2019) 338.
[30] Y. Zhang, G. Li, J. Wang, G. Cui, X. Wei, L. Shui, K. Kempa, G. Zhou, X. Wang, Z. Chen, Adv. Funct. Mater. 30 (2020) 2001165.
[31] X. Li, Y. Zhang, S. Wang, Y. Liu, Y. Ding, G. He, N. Zhang, G. Yu, Nano Lett. 20 (2020) 701.
[32] X.H. Li, S. Kurasch, U. Kaiser, M. Antonietti, Angew. Chem. Int. Ed. 51 (2012) 9689.
[33] Y. Chen, S. Ji, Y. Wang, J. Dong, W. Chen, Z. Li, R. Shen, L. Zheng, Z. Zhuang, D. Wang, Y. Li, Angew. Chem. Int. Ed. 56 (2017) 6937.
[34] M. Zhang, Y.G. Wang, W. Chen, J. Dong, L. Zheng, J. Luo, J. Wan, S. Tian, W.C. Cheong, D. Wang, Y. Li, J. Am. Chem. Soc. 139 (2017) 10976.
[35] G. Zhou, S. Zhao, T. Wang, S. Yang, B. Johannessen, H. Chen, C. Liu, Y. Ye, Y. Wu, Y. Peng, C. Liu, S.P. Jiang, Q. Zhang, Y. Cui, Nano Lett. 20 (2020) 1252.
[36] D. Wang, J. Zhou, Y. Hu, J. Yang, N. Han, Y. Li, T.-K. Sham, J. Phys. Chem. C 119 (2015) 19573.
[37] J. Jiang, F. Sun, S. Zhou, W. Hu, H. Zhang, J. Dong, Z. Jiang, J. Zhao, J. Li, W. Yan, M. Wang, Nat. Commun. 9 (2018) 2885.
[38] Z. Yu, B. Wang, X. Liao, K. Zhao, Z. Yang, F. Xia, C. Sun, Z. Wang, C. Fan, J. Zhang, Y. Wang, Adv. Energy Mater. 10 (2020) 2000907.
[39] S. Li, W. Zhang, Z. Zeng, S. Cheng, J. Xie, Electrochem. Energy Rev. 3 (2020) 613.
[40] D.R. Deng, F. Xue, C.D. Bai, J. Lei, R. Yuan, M.S. Zheng, Q.F. Dong, ACS Nano 12 (2018) 11120.
[41] D. Fang, Y. Wang, C. Qian, X. Liu, X. Wang, S. Chen, S. Zhang, Adv. Funct. Mater. 29 (2019) 1900875.
[42] Y. Song, W. Zhao, L. Kong, L. Zhang, X. Zhu, Y. Shao, F. Ding, Q. Zhang, J. Sun, Z. Liu, Energy Environ. Sci. 11 (2018) 2620.
[43] M. Zhao, H.J. Peng, B. Li, X. Chen, J. Xie, X. Liu, Q. Zhang, J.Q. Huang, Angew. Chem. Int. Ed. 132 (2020) 9096.